



Contents lists available at ScienceDirect



Catalysis Today

journal homepage: www.elsevier.com/locate/cattod

Three-dimensionally ordered macroporous CoCr_2O_4 -supported Au–Pd alloy nanoparticles: Highly active catalysts for methane combustion

Zhiwei Wang, Jiguang Deng*, Yuxi Liu, Huanggen Yang, Shaohua Xie, Zhixing Wu, Hongxing Dai*

Beijing Key Laboratory for Green Catalysis and Separation, Key Laboratory of Beijing on Regional Air Pollution Control, Key Laboratory of Advanced Functional Materials, Education Ministry of China, and Laboratory of Catalysis Chemistry and Nanoscience, Department of Chemistry and Chemical Engineering, College of Environmental and Energy Engineering, Beijing University of Technology, Beijing 100124, China

ARTICLE INFO

Article history:

Received 5 January 2016

Received in revised form 11 April 2016

Accepted 11 May 2016

Available online xxx

Keywords:

Three-dimensionally ordered macropore

Au–Pd alloy nanoparticle

Cobalt chromate

Supported noble metal catalyst

Methane combustion

ABSTRACT

Three-dimensionally ordered macroporous CoCr_2O_4 (3DOM CoCr_2O_4) and its supported Au–Pd alloy ($x\text{AuPd}_y/3\text{DOM CoCr}_2\text{O}_4$; $x=0.98$ and 1.93 wt%; Pd/Au molar ratio (y) = 1.93 – 1.96) nanocatalysts were prepared using the polymethyl methacrylate-templating and polyvinyl alcohol-protected reduction methods, respectively. Physicochemical properties of the samples were characterized by means of a number of techniques, and their catalytic activities were evaluated for methane combustion. The 3DOM CoCr_2O_4 and $x\text{AuPd}_y/3\text{DOM CoCr}_2\text{O}_4$ samples possessed a high-quality 3DOM structure and a surface area of 33 – $36 \text{ m}^2/\text{g}$. The Au–Pd alloy nanoparticles (NPs) with an average size of 3.3 nm were uniformly dispersed on the surface of the samples. The $1.93\text{AuPd}_{1.95}/3\text{DOM CoCr}_2\text{O}_4$ sample showed the best catalytic performance: the $T_{10\%}$, $T_{50\%}$, and $T_{90\%}$ (temperatures required for achieving methane conversion of 10 , 50 , and 90% , respectively) were 305 , 353 , and 394°C at a space velocity (SV) of $20,000 \text{ mL}/(\text{g}\cdot\text{h})$. The effects of SV, water vapor, and sulfur dioxide on the catalytic activity of the $1.93\text{AuPd}_{1.95}/3\text{DOM CoCr}_2\text{O}_4$ sample were also examined. It is concluded that the excellent catalytic performance of $1.93\text{AuPd}_{1.95}/3\text{DOM CoCr}_2\text{O}_4$ was associated with the higher surface area and adsorbed oxygen species concentration, better low-temperature reducibility, and strong interaction between Au–Pd alloy NPs and 3DOM CoCr_2O_4 .

© 2016 Elsevier B.V. All rights reserved.

1. Introduction

As the main component of natural gas, methane is widely used in the field of chemical industry, transportation, and private families. In the traditional applications, however, methane combustion usually undertakes above 1200°C , and this combustion process inevitably gives rise to harmful gases, such as NO_x and CO, which can cause serious pollution to the atmosphere environment. Catalytic combustion of methane is an effective pathway to decrease the emissions of NO_x and CO, in which the key issue is the availability of high-performance catalysts.

Supported noble metal Pd or Pt shows excellent catalytic performance at low temperatures for methane combustion [1]. For instance, Li et al. [2] reported that Co_3O_4 nanosheet-supported 5 wt\% Pd exhibited a high activity for methane combustion due to the strong interaction between Pd^{2+} and Co_3O_4 . Xu et al. [3] pointed out that the good performance of $\text{Pd}/\gamma\text{-Al}_2\text{O}_3$ for methane com-

bustion was due to the formation of PdO_x at the top layers above 250°C . Although some noble metals are expensive, one can insert a less cheap metal to form a bimetal alloy catalyst. Au is an ideal candidate. The addition of Au to Pd could greatly enhance the catalytic activity and stability. In recent years, some researchers observed that Au–Pd alloys were highly active in the combustion of toluene, alcohols, and methane [4–7]. For example, Goodman et al. [6] investigated the promotional effect of Au in the Au–Pd alloy catalyst, and found that the Au could isolate the Pd site. After studying the Au-Pd/TiO_2 catalysts for the solvent-free oxidation of primary alcohols to aldehydes, Hutchings et al. [7] pointed out that the Au could act as an electronic promoter for Pd.

Transition-metal (e.g., Mn, Co, Cr and Fe) oxides [8–10] are generally considered as efficient catalyst support because of lower cost and relative abundant resources. Among the transition-metal oxide catalysts, Cr-based spinel-type oxides (e.g., CoCr_2O_4) exhibit fair catalytic activities in dichloromethane oxidation [11], NO_x removal [12], and methane combustion [13–15]. Li et al. [14] observed that cobalt–chromium oxide with the cobalt/chromium atomic ratio of $1:2$ exhibited good performance for methane combustion. However, their cobalt–chromium oxide catalysts were

* Corresponding authors.

E-mail addresses: jgdeng@bjut.edu.cn (J. Deng), hxdai@bjut.edu.cn (H. Dai).

irregular in morphology and no presence of pores. In the past years, three-dimensionally ordered macroporous (3DOM) materials have been intensively studied for the applications in various fields (such as semiconducting, photonics, electrochromics, and catalysis [16–18]), because they have several advantages of higher surface areas, easy mass transfer, and suitability for dispersion of active components. To the best of our knowledge, there have so far been no reports on the preparation and catalytic activities of 3DOM CoCr_2O_4 -supported Au–Pd alloy nanoparticles (NPs) for methane combustion in the literature.

Previously, our group prepared the 3DOM or three-dimensionally ordered mesoporous cobalt oxide-supported gold-palladium alloy nanocatalysts, and investigated their catalytic performance for the oxidation of carbon dioxide, toluene, and methane [19–21]. It is found that the optimal gold/palladium atomic ratio was ca. 1:2. In the present study, we adopted the polymethyl methacrylate (PMMA)-templating and polyvinyl alcohol (PVA)-protected reduction strategies to generate the 3DOM CoCr_2O_4 and $x\text{AuPd}_y/3\text{DOM CoCr}_2\text{O}_4$ nanocatalysts, characterized their physicochemical properties, and evaluated their catalytic activities for methane combustion.

2. Experimental

2.1. Catalyst preparation

The well-arrayed PMMA microspheres with an average diameter of ca. 300 nm were synthesized according to procedures described elsewhere [22].

The 3DOM CoCr_2O_4 was prepared via the PMMA-templating route. In a typical procedure, 6.66 mmol of $\text{Co}(\text{NO}_3)_2 \cdot 6\text{H}_2\text{O}$ and 13.3 mmol of $\text{Cr}(\text{NO}_3)_3 \cdot 9\text{H}_2\text{O}$ were dissolved in 10 mL of poly(ethylene glycol) (PEG, MW = 400 g/mol) and methanol (MeOH) solution (PEG/MeOH volumetric ratio = 1:9) at room temperature (RT) under stirring for 30 min to obtain a transparent solution. Then, 2.0 g of the PMMA hard template was soaked in the above precursor solution for about 30 min. After that, the mixture was filtered and dried at RT for 48 h. The as-obtained powders were calcined in a N_2 flow of 100 mL/min at a ramp of 1 $^{\circ}\text{C}/\text{min}$ from RT to 300 $^{\circ}\text{C}$ and maintained at this temperature for 2 h, then cooled to RT, and calcined in an air flow of 100 mL/min at a ramp of 1 $^{\circ}\text{C}/\text{min}$ from RT to 300 $^{\circ}\text{C}$ and maintained at this temperature for 2 h, and finally increased to 500 $^{\circ}\text{C}$ and maintained at this temperature for 4 h, thus generating the 3DOM CoCr_2O_4 sample.

The 3DOM CoCr_2O_4 -supported gold-palladium alloy ($x\text{AuPd}_y/3\text{DOM CoCr}_2\text{O}_4$) samples were prepared using the PVA-protected reduction method. The typical preparation procedure was as follows: 1.8 and 3.6 mL (for $x=0.98$ and 1.93 wt%, respectively) of PVA aqueous solution (2.0 g/L) was added to PdCl_2 (1.5 mmol/L) and HAuCl_4 (1.5 mmol/L) mixed aqueous solution in an ice bath under vigorous stirring for 30 min. Then, 2.1 and 4.1 mL (for $x=0.98$ and 1.93 wt%, respectively) of NaBH_4 aqueous solution (2.0 g/L) was quickly injected into the mixed noble metal aqueous solution, generating a dark-brown sol. Subsequently, 0.3 g of the 3DOM CoCr_2O_4 support was then added to the dark-brown sol and vigorously stirred for 6 h. Afterwards, the mixture solution was filtered and washed with deionized water until there was no Cl^- ions in the supernatant were detected using an AgNO_3 aqueous solution (0.1 mol/L). The obtained wet solid was dried at 80 $^{\circ}\text{C}$ for 10 h, and calcined in a muffle furnace at a ramp of 1 $^{\circ}\text{C}/\text{min}$ from RT to 500 $^{\circ}\text{C}$ and maintained at this temperature for 4 h, thus obtaining the $x\text{AuPd}_y/3\text{DOM CoCr}_2\text{O}_4$ samples. The results of inductively coupled plasma atomic emission spectroscopic (ICP-AES) investigations reveal that the real loadings of noble metals

were 0.98 and 1.93 wt% in $x\text{AuPd}_y/3\text{DOM CoCr}_2\text{O}_4$, respectively, and the corresponding real Pd/Au molar ratios were 1.93 and 1.95.

For comparison, the Bulk CoCr_2O_4 and $x\text{AuPd}_y/\text{Bulk CoCr}_2\text{O}_4$ samples were also prepared using the above same methods without adding the PMMA template. The results of the ICP-AES studies reveal that the real Au–Pd loading (x) was 1.98 wt% in the $x\text{AuPd}_y/\text{Bulk CoCr}_2\text{O}_4$ sample, with the real Pd/Au molar ratio being 1.96.

All chemicals (A.R. in purity) were purchased from Beijing Chemical Reagent Company and used without further purification.

2.2. Catalyst characterization

Elemental analyses of the noble metal loadings were performed using the ICP-AES technique on a Thermo Electron IRIS Intrepid ER/S spectrometer. X-ray diffraction (XRD) patterns of the samples were recorded on a Bruker D8 Advance diffractometer with $\text{Cu K}\alpha$ radiation and nickel filter ($\lambda=0.15406\text{ nm}$). Scanning electron microscopic (SEM) images of the samples were recorded on a Gemini Zeiss Supra 55 apparatus (operating at 10 kV). Transmission electron microscopic (TEM) images and selected-area electron diffraction (SAED) patterns of the samples were obtained using the JEOL-2010 equipment (operating at 200 kV). BET (Brunauer–Emmett–Teller) surface areas and pore-size distributions of the samples were measured via N_2 adsorption at –196 $^{\circ}\text{C}$ on a Micromeritics ASAP 2020 analyzer with the samples being degassed at 250 $^{\circ}\text{C}$ for 2.5 h under vacuum before measurement. X-ray photoelectron spectroscopy (XPS, VG CLAM 4 MCD analyzer) was used to determine the Co 2p, O 1s, Au 4f, Pd 3d, and C 1s binding energies (BEs) of surface species using $\text{Mg K}\alpha$ ($h\nu=1253.6\text{ eV}$) as the excitation source.

Hydrogen temperature-programmed reduction (H_2 -TPR) experiments were carried out on a chemical adsorption analyzer (Autochem II 2920, Micromeritics). Before TPR measurement, ca. 50 mg of the sample (40–60 mesh) was loaded to a quartz fixed-bed U-shaped microreactor (i.d. = 4 mm) and pretreated in an O_2 flow of 20 mL/min at 300 $^{\circ}\text{C}$ for 1 h. After being cooled at the same atmosphere to RT, the sample was purged with a helium flow of 30 mL/min for 15 min. Finally, the pretreated sample was exposed to a flow (50 mL/min) of 5% H_2 –95% Ar (v/v) mixture and heated at a ramp of 10 $^{\circ}\text{C}/\text{min}$ from RT to 900 $^{\circ}\text{C}$. The alteration in H_2 concentration of the effluent was monitored online by the chemical adsorption analyzer. The reduction peak was calibrated against that of the complete reduction of a known standard powdered CuO (Aldrich, 99.995%).

2.3. Catalytic evaluation

Catalytic activities of the samples were evaluated in a continuous flow fixed-bed quartz tubular microreactor (i.d. = 6.0 mm). 50 mg of the sample (40–60 mesh) was diluted with 0.25 g of quartz sands (40–60 mesh). Prior to the measurement, the sample was pretreated in an O_2 flow of 20 mL/min at 300 $^{\circ}\text{C}$ for 1 h. After being cooled to a given temperature, the reactant gas containing methane was passed through the catalyst bed. The reactant mixture gas was 2.5 vol% CH_4 + 20 vol% O_2 + 77.5 vol% N_2 (balance), and the total flow was 16.7 mL/min, giving a space velocity (SV) of ca. 20,000 mL/(g h). In the case of water vapor introduction, 5.0 vol% H_2O was introduced by passing the feed stream through a water saturator at a certain temperature. In the case of SO_2 introduction, 100-ppm SO_2 from a SO_2 cylinder (balanced with N_2) was introduced to the reaction system through a mass flow controller. Reactants and products were analyzed online by gas chromatography (GC-14C, Shimadzu) equipped with a flame ionization detector (FID) and a thermal conductivity detector (TCD), using a stabilwax column (30 m in length) for methane separation and a Carboxen

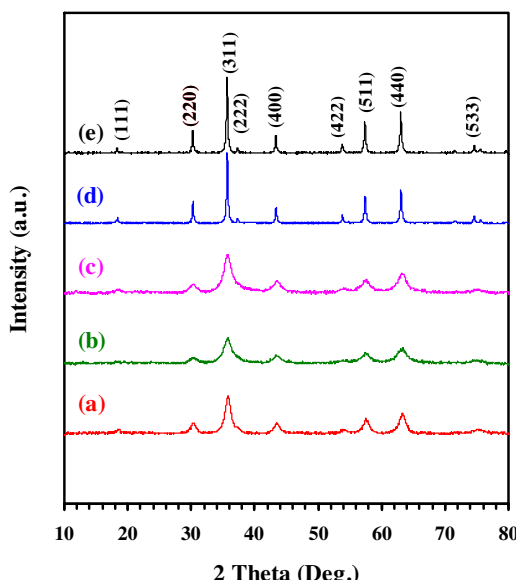


Fig. 1. XRD patterns of (a) 3DOM CoCr₂O₄, (b) 0.98AuPd_{1.93}/3DOM CoCr₂O₄, (c) 1.93AuPd_{1.95}/3DOM CoCr₂O₄, (d) 1.98AuPd_{1.96}/Bulk Co₃O₄, and (e) Bulk CoCr₂O₄.

1000 column (3 m in length) for permanent gas detection. The balance of carbon throughout the catalytic system was estimated to be $99.5 \pm 1.5\%$. Catalytic activities of the samples were evaluated using the temperatures ($T_{10\%}$, $T_{50\%}$, and $T_{90\%}$) required for achieving methane conversions of 10, 50, and 90%, respectively. CH₄ conversion was defined as $(c_{\text{inlet}} - c_{\text{outlet}})/c_{\text{inlet}} \times 100\%$, where the c_{inlet} and c_{outlet} are CH₄ concentrations of the inlet and outlet feed stream, respectively.

3. Results and discussion

3.1. Catalyst composition, crystal structure, morphology, particle size distribution, and surface area

The results of ICP-AES investigations reveal that the chemical compositions of xAuPdy/3DOM CoCr₂O₄ and xAuPdy/Bulk CoCr₂O₄ samples were 0.98 wt% AuPd_{1.93}/3DOM CoCr₂O₄, 1.93 wt% AuPd_{1.95}/3DOM CoCr₂O₄, and 1.98 wt% AuPd_{1.96}/Bulk CoCr₂O₄ (denoted as 0.98AuPd_{1.93}/3DOM CoCr₂O₄, 1.93AuPd_{1.95}/3DOM CoCr₂O₄, and 1.98AuPd_{1.96}/Bulk CoCr₂O₄), respectively.

Fig. 1 shows the XRD patterns of the as-prepared samples. Compared to the XRD pattern of the standard CoCr₂O₄ sample (JCPDS PDF # 22-1084), one can realize that the CoCr₂O₄ in Bulk CoCr₂O₄, 1.98AuPd_{1.96}/Bulk CoCr₂O₄ or xAuPdy/3DOM CoCr₂O₄ was cubic in crystal structure, and all of the Bragg diffraction peaks could be well indexed, as indicated in Fig. 1e. The loading of Au–Pd alloys did not lead to any changes in crystal structure of CoCr₂O₄. No Au,

Pd or Au–Pd alloy phases were detected, indicating that the noble metal NPs were highly dispersed on the surface of the samples. No detection of noble metal phases might be also due to their lower loadings.

Fig. 2 shows the SEM images of the porous samples. It can be clearly seen that the 3DOM CoCr₂O₄ and xAuPdy/3DOM CoCr₂O₄ samples displayed a high-quality 3DOM architecture with a macropore diameter of 120–180 nm. The loading of Au–Pd NPs did not destroy the macropore structure of CoCr₂O₄. Fig. 3 shows the TEM images and SAED patterns of the xAuPdy/3DOM CoCr₂O₄ and 1.98AuPd_{1.96}/Bulk CoCr₂O₄ samples. Apparently, the xAuPdy/3DOM CoCr₂O₄ samples possessed a high-quality 3DOM structure that was composed of interconnected macropores with nanocrystalline skeletons, in agreement with their SEM observations; however, the 1.98AuPd_{1.96}/Bulk CoCr₂O₄ sample exhibited a sub-microsized morphology. The Au–Pd alloy NPs were uniformly deposited on the surface of the samples. The sizes of Au–Pd alloy NPs were in the range of 2–6 nm. After statistical analysis on the sizes of 100 Au–Pd alloy NPs in the TEM images of the samples, the particle size distributions of noble metal NPs are shown in Fig. 4. The average sizes of noble metal NPs in 0.98AuPd_{1.93}/3DOM CoCr₂O₄, 1.93AuPd_{1.95}/3DOM CoCr₂O₄, and 1.98AuPd_{1.96}/Bulk CoCr₂O₄ were 3.3, 3.4, and 3.5 nm, respectively. The recording of multiple bright electron diffraction rings in the SAED patterns (Fig. 3) of the 0.98AuPd_{1.93}/3DOM CoCr₂O₄, 1.93AuPd_{1.95}/3DOM CoCr₂O₄, and 1.98AuPd_{1.96}/Bulk CoCr₂O₄ samples reveals that these materials were polycrystalline.

Fig. 5 shows the N₂ adsorption-desorption isotherms and pore-size distributions of the samples, and their textural properties are summarized in Table 1. It can be observed from Fig. 5A that all of the samples displayed a type II isotherm with a type H3 hysteresis loop in the relative pressure (p/p_0) range of 0.8–1.0, indicating that these samples possessed a macroporous structure. The pore-size distribution curves showed that each of the samples possessed a pore-size distribution in the ranges of 2–8 and 50–180 nm, respectively. The BET surface areas of the porous samples (3DOM CoCr₂O₄, 0.98AuPd_{1.93}/3DOM CoCr₂O₄, and 1.93AuPd_{1.95}/3DOM CoCr₂O₄) were 33.2–35.6 m²/g, significantly higher than those (7.2–8.8 m²/g) of the bulk counterparts (Bulk CoCr₂O₄ and 1.98AuPd_{1.96}/Bulk CoCr₂O₄).

3.2. Surface composition, metal oxidation state, and oxygen species

XPS is an effective technique to investigate the surface element compositions, metal oxidation states, and adsorbed species of a catalyst. Fig. 6 shows the Co 2p_{3/2}, Cr 2p_{3/2}, O 1s, Au 4f, and Pd 3d XPS spectra of the samples. The asymmetrical Co 2p_{3/2} XPS spectrum of each sample could be decomposed to two components at BE = 780.7 and 783.1 eV (Fig. 6A), assignable to the surface Co³⁺ and Co²⁺ species [23], respectively. The presence of surface Co²⁺ in the samples was also confirmed by the recording of a satellite signal at

Table 1

BET surface areas, pore diameters, pore volumes, average Au–Pd particle sizes, real Au and Pd contents, and real Pd/Au molar ratios of the as-prepared samples.

| Sample | Surface area (m ² /g) | Pore diameter ^a (nm) | Pore volume (cm ³ /g) | Average Au–Pd particle size ^b (nm) | Real Au content ^c (wt%) | Real Pd content ^c (wt%) | Real Pd/Au molar ratio ^c (mol/mol) |
|---|----------------------------------|---------------------------------|----------------------------------|---|------------------------------------|------------------------------------|---|
| 3DOM CoCr ₂ O ₄ | 33.2 | 120–180 | 0.029 | — | — | — | — |
| 0.98AuPd _{1.93} /3DOM CoCr ₂ O ₄ | 35.6 | 120–180 | 0.031 | 3.2 | 0.48 | 0.50 | 1.93 |
| 1.93AuPd _{1.95} /3DOM CoCr ₂ O ₄ | 34.9 | 120–180 | 0.033 | 3.3 | 0.94 | 0.99 | 1.95 |
| 1.98AuPd _{1.96} /Bulk CoCr ₂ O ₄ | 8.8 | — | — | 3.2 | 0.96 | 1.02 | 1.96 |
| Bulk CoCr ₂ O ₄ | 7.2 | — | — | — | — | — | — |

^a Data were estimated according to the estimation of macropores in the SEM images of the samples.

^b Data were estimated according to the estimation of noble metal particles in the TEM images of the samples.

^c Data were determined by the ICP-AES technique.

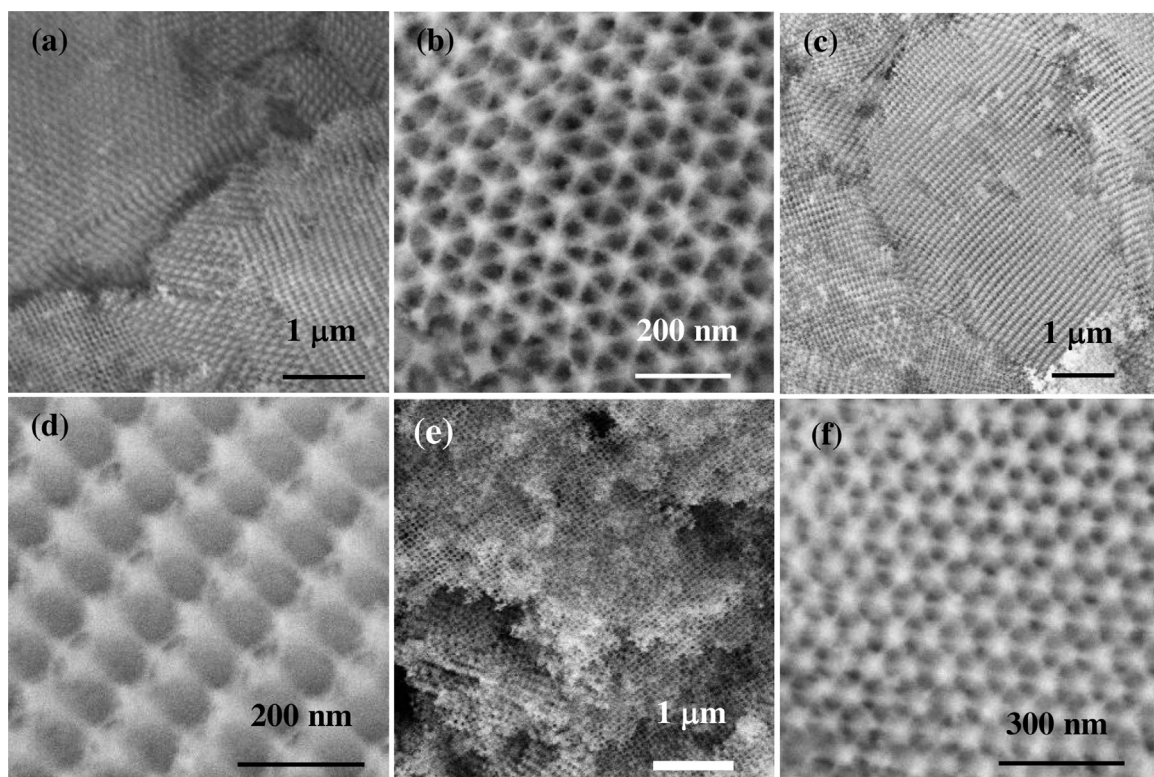


Fig. 2. SEM images of (a, b) 3DOM CoCr_2O_4 , (c, d) 0.98AuPd_{1.85}/3DOM CoCr_2O_4 , and (e, f) 1.93AuPd_{1.95}/3DOM CoCr_2O_4 .

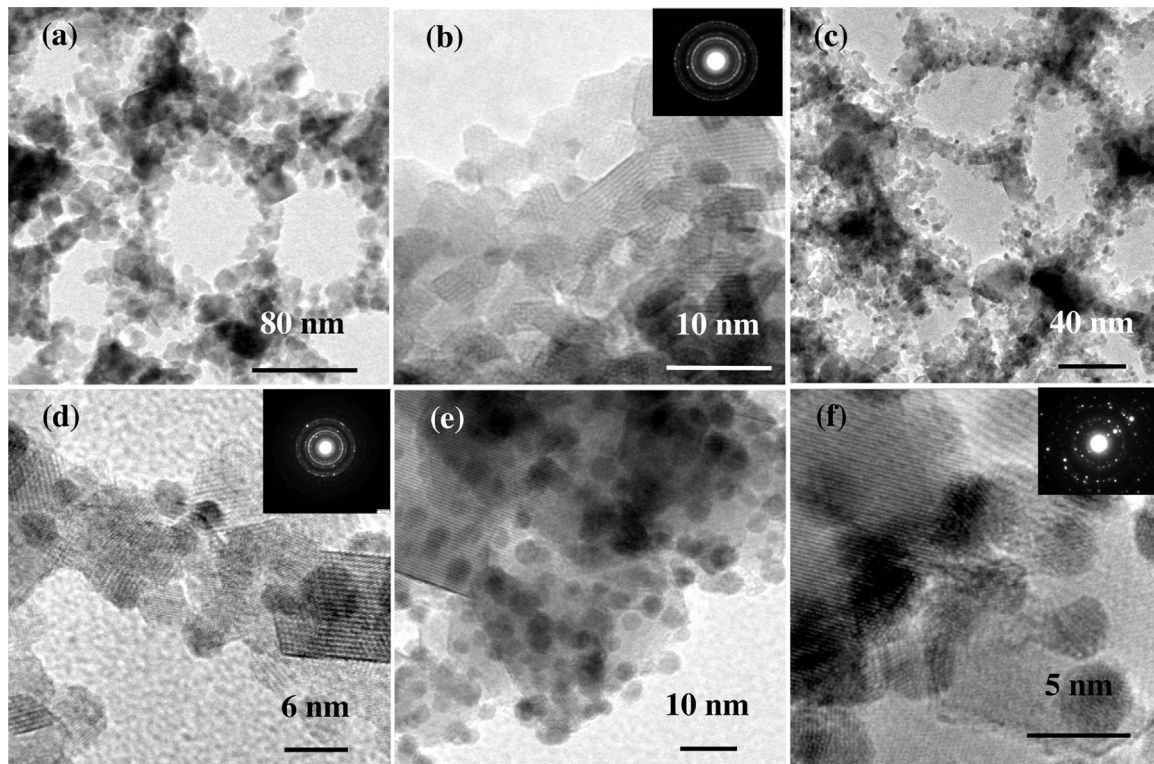


Fig. 3. TEM images and SAED patterns (insets) of (a, b) 0.98AuPd_{1.85}/3DOM CoCr_2O_4 , (c, d) 1.93AuPd_{1.95}/3DOM CoCr_2O_4 , and (e, f) 1.98AuPd_{1.96}/Bulk CoCr_2O_4 .

$\text{BE} = 787.2 \text{ eV}$. The surface $\text{Co}^{3+}/\text{Co}^{2+}$ molar ratios of the samples are summarized in Table 2. The surface $\text{Co}^{3+}/\text{Co}^{2+}$ molar ratio significantly decreased from 2.95 to 1.92–2.24 after the loading of Au–Pd alloy NPs. In other words, the 3DOM CoCr_2O_4 in the supported

Au–Pd alloy samples would possess higher oxygen vacancy concentrations in the surface vicinity of 3DOM CoCr_2O_4 [24]. The Cr 2p_{3/2} XPS spectrum of each sample could be decomposed into three components at $\text{BE} = 575.4$, 576.5, and 578.2 eV (Fig. 6B), attributable to

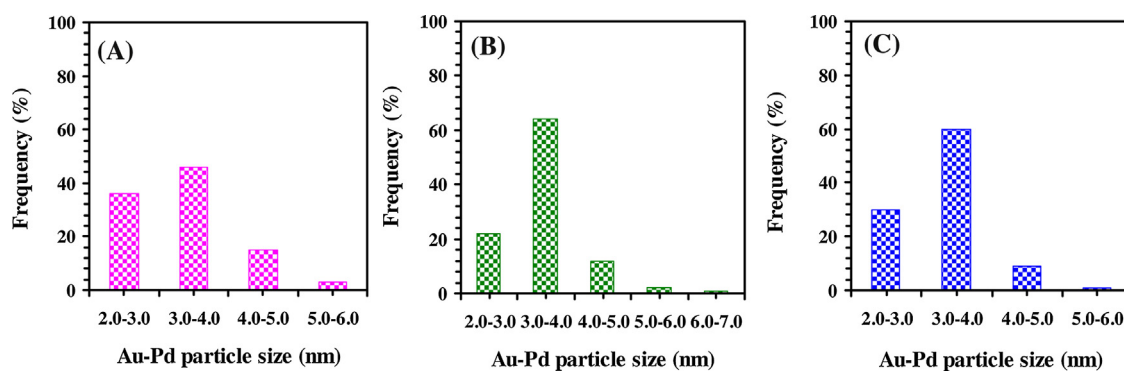


Fig. 4. Au Pd particle size distributions of (A) 0.98AuPd_{1.93}/3DOM CoCr₂O₄, (B) 1.93AuPd_{1.95}/3DOM CoCr₂O₄, and (C) 1.98AuPd_{1.96}/Bulk CoCr₂O₄.

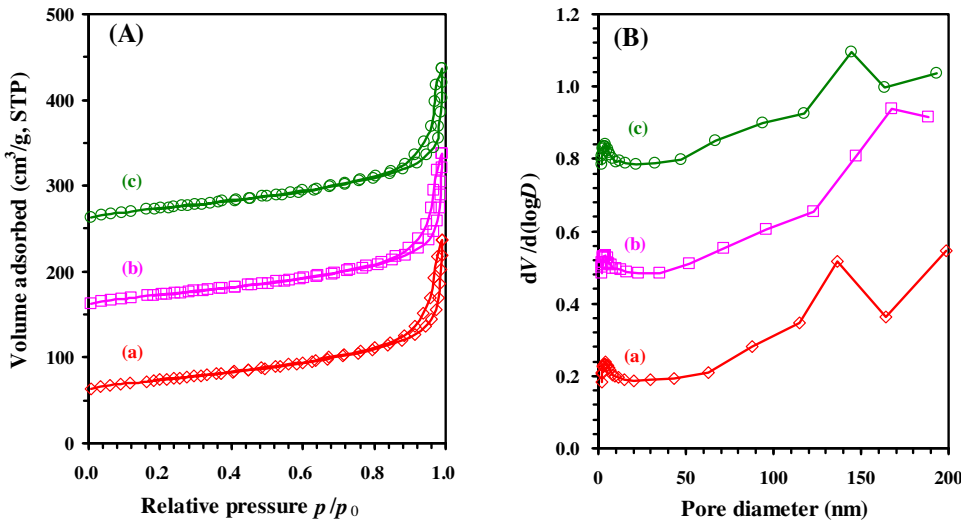


Fig. 5. (A) N₂ adsorption desorption isotherms and (B) pore-size distributions of (a) 3DOM CoCr₂O₄, (b) 0.98AuPd_{1.93}/3DOM CoCr₂O₄ and (c) 1.93AuPd_{1.95}/3DOM CoCr₂O₄.

Table 2
Surface element compositions and H₂ consumption of the samples.

| Sample | Co ³⁺ /Co ²⁺ molar ratio (mol/mol) | Cr ⁶⁺ /Cr ³⁺ molar ratio (mol/mol) | O _{ads} /O _{latt} molar ratio (mol/mol) | Au ^{δ+} /Au ⁰ molar ratio (mol/mol) | Pd ²⁺ /Pd ⁰ molar ratio (mol/mol) | H ₂ consumption below 400 °C ^a (mmol/g) |
|---|--|--|---|---|---|---|
| 3DOM CoCr ₂ O ₄ | 2.95 | 0.54 | 0.53 | — | — | 0.25 |
| 0.98AuPd _{1.93} /3DOM CoCr ₂ O ₄ | 2.20 | 0.38 | 0.55 | 0.09 | 0.11 | 0.40 |
| 1.93AuPd _{1.95} /3DOM CoCr ₂ O ₄ | 1.92 | 0.39 | 0.62 | 0.17 | 0.23 | 0.66 |
| 1.98AuPd _{1.96} /Bulk CoCr ₂ O ₄ | 2.24 | 0.39 | 0.60 | 0.12 | 0.20 | 0.17 |
| Bulk CoCr ₂ O ₄ | — | — | — | — | — | 0.34 |

^a Data were estimated by quantitatively analyzing the reduction peaks in the H₂-TPR profiles.

the surface Cr(OH)₃ or Cr₂O₃ [25], Cr³⁺ (occupied octahedral sites) [11,14,26], and Cr⁶⁺ [14,27,28] species, respectively. The Cr⁶⁺/Cr³⁺ molar ratio decreased from 0.54 to 0.38–0.39 (Table 2) when the Au–Pd alloy NPs were loaded on the surface of 3DOM CoCr₂O₄ or Bulk CoCr₂O₄.

As shown in Fig. 6C, the asymmetric O 1s XPS signal could be deconvoluted to three components at BE = 530.1, 531.6, and 532.9 eV, ascribable to the surface lattice oxygen (O_{latt}), adsorbed oxygen (O_{ads}, e.g., O₂[−], O₂^{2−} or O[−]), and carbonate or adsorbed water species [29,30], respectively. It has been known that the surface adsorbed oxygen species play an important role in deep oxidation of organics [29]. With the loading of Au–Pd alloy NPs, the surface O_{ads}/O_{latt} molar ratio increased and the 1.93AuPd_{1.95}/3DOM CoCr₂O₄ sample possessed the highest O_{ads}/O_{latt} molar ratio (0.62).

The Au 4f XPS spectrum of each sample could be decomposed into four components at BE = 83.5, 84.5, 87.2, and 88.3 eV (Fig. 6D).

The components at BE = 83.5 and 87.2 eV were assigned to the surface metallic gold (Au⁰) species, whereas the ones at BE = 84.5 and 88.3 eV were attributed to the surface oxidized gold (Au^{δ+}) species [31,32]. As shown in Fig. 6E, the Pd 3d spectrum of each sample could be deconvoluted into four components at BE = 335.5, 337.9, 340.9, and 343.2 eV. The components at BE = 335.5 and 340.9 eV were due to the surface metallic palladium (Pd⁰) species, while the ones at BE = 337.9 and 343.2 eV were due to the surface oxidized palladium (Pd²⁺) species [33]. Apparently, the Au^{δ+}/Au⁰ or Pd²⁺/Pd⁰ molar ratio increased with the loading of Au–Pd alloy NPs, a result possibly due to the strong interaction between noble metal NPs and cobalt–chromium oxide (Au⁰ or Pd⁰ + Co³⁺ → Au^{δ+} or Pd²⁺ + Co²⁺; Au⁰ or Pd⁰ + Cr⁶⁺ → Au^{δ+} or Pd²⁺ + Cr³⁺) [31,34], which coincides with the drop in surface Co³⁺/Co²⁺ or Cr⁶⁺/Cr³⁺ molar ratio of the samples.

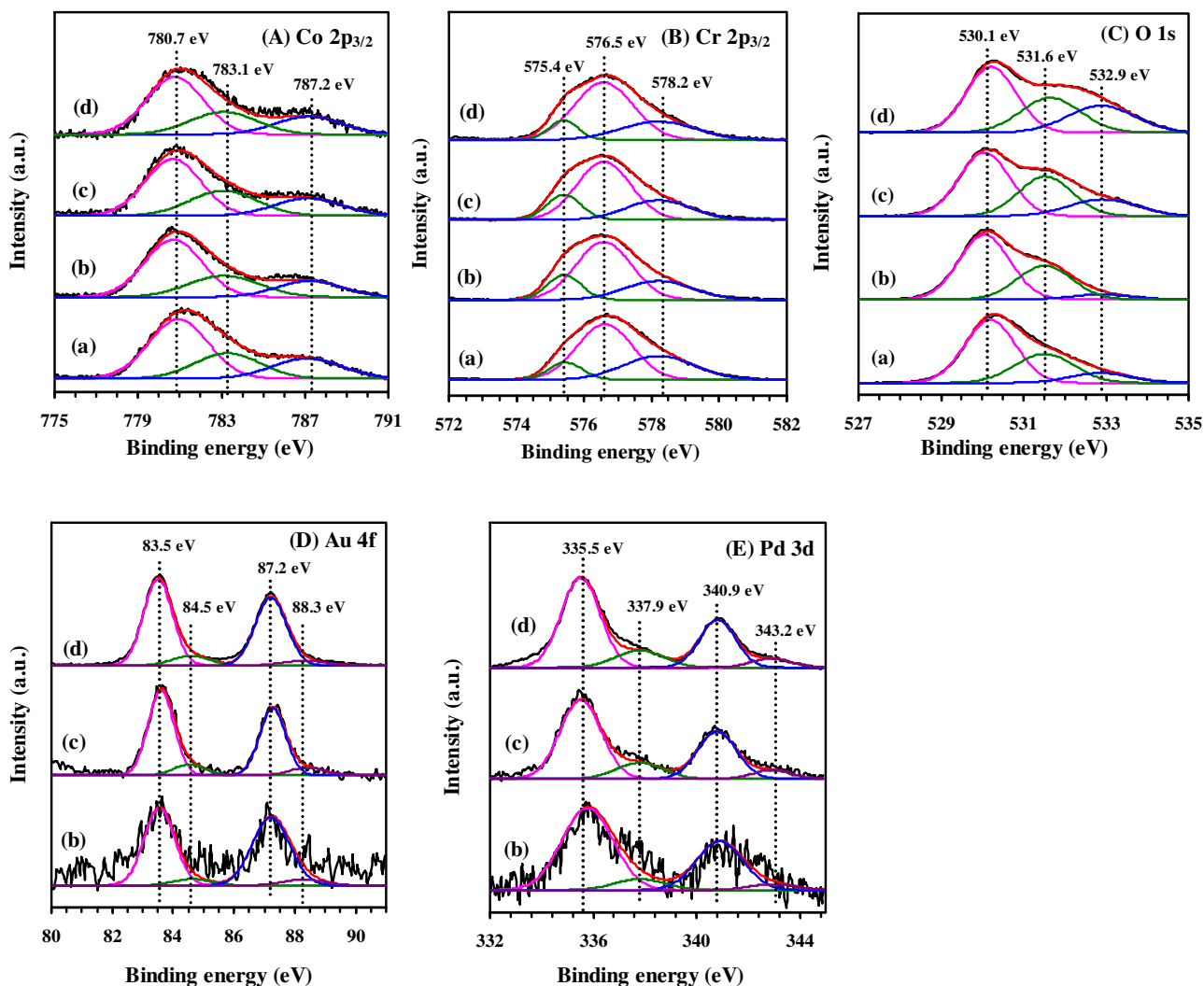


Fig. 6. (A) Co 2p_{3/2}, (B) Cr 2p_{3/2}, (C) O 1s, (D) Au 4f, and (E) Pd 3d XPS spectra of (a) 3DOM CoCr₂O₄, (b) 0.98AuPd_{1.93}/3DOM CoCr₂O₄, (c) 1.93AuPd_{1.95}/3DOM CoCr₂O₄, and (d) 1.98AuPd_{1.96}/Bulk CoCr₂O₄.

3.3. Reducibility

H₂-TPR experiments were performed to investigate the reducibility of the catalysts, and the results are illustrated in Fig. 7A. For the 3DOM CoCr₂O₄ sample, there were three reduction peaks at 282, 467, and 723 °C. According to the literature, the reduction peak centered at 723 °C was assigned to the reduction of Co²⁺ to the metallic cobalt [35]. The reduction peaks at 282 and 467 °C were attributed to the reduction of Cr⁶⁺ to Cr³⁺ at the surface and bulk of CoCr₂O₄ [36,37], respectively. Comparing to the Bulk CoCr₂O₄, the 3DOM CoCr₂O₄ sample was more reducible at lower temperatures. After loading the Au-Pd NPs on the 3DOM CoCr₂O₄ surface, the reduction peaks of the xAuPdy/3DOM CoCr₂O₄ and 1.98AuPd_{1.96}/Bulk CoCr₂O₄ samples shifted to lower temperatures. The first reduction peak was assignable to the reduction of cationic Au or Pd and surface adsorbed oxygen species.

By quantitatively analyzing the reduction peaks in the H₂-TPR profiles, one can obtain the H₂ consumption of the samples, as summarized in Table 2. Apparently, the H₂ consumptions of the xAuPdy/3DOM CoCr₂O₄ and 1.98AuPd_{1.96}/Bulk CoCr₂O₄ samples were higher than those of the 3DOM CoCr₂O₄ and Bulk CoCr₂O₄ supports. Generally speaking, the initial (where less than 25% oxygen in the sample is consumed for the first reduction peak) H₂ consumption rate can be used to evaluate the low-temperature

reducibility of a sample [38], and the results are shown in Fig. 7B. Obviously, the low-temperature reducibility decreased in the order of 1.93AuPd_{1.95}/3DOM CoCr₂O₄ > 0.98AuPd_{1.93}/3DOM CoCr₂O₄ > 3DOM CoCr₂O₄ > 1.98AuPd_{1.96}/Bulk CoCr₂O₄ > Bulk CoCr₂O₄, which was basically in agreement with the sequence in catalytic activity (shown below).

3.4. Catalytic performance

Catalytic activities of the as-prepared samples were evaluated for methane combustion, and the results are shown in Fig. 8A. It is observed that the 3DOM CoCr₂O₄ and xAuPdy/3DOM CoCr₂O₄ samples performed much better than the Bulk CoCr₂O₄ and 1.98AuPd_{1.96}/Bulk CoCr₂O₄ samples, respectively. Compared to the bulk sample, the 3DOM-structured catalysts displayed porous structures and much higher surface areas. Generally speaking, combustion of methane takes place on the surface of a catalyst. A porous structure is beneficial for the dispersion of active components as well as the adsorption and diffusion of reactants, whereas a higher surface area can favor the accessibility of reactants to the surface active sites [18]. Therefore, it is understandable that the 3DOM-structured catalysts outperformed the bulk counterpart. Furthermore, the loading of Au-Pd alloy NPs were beneficial for the enhancement in catalytic performance of the sample. To better

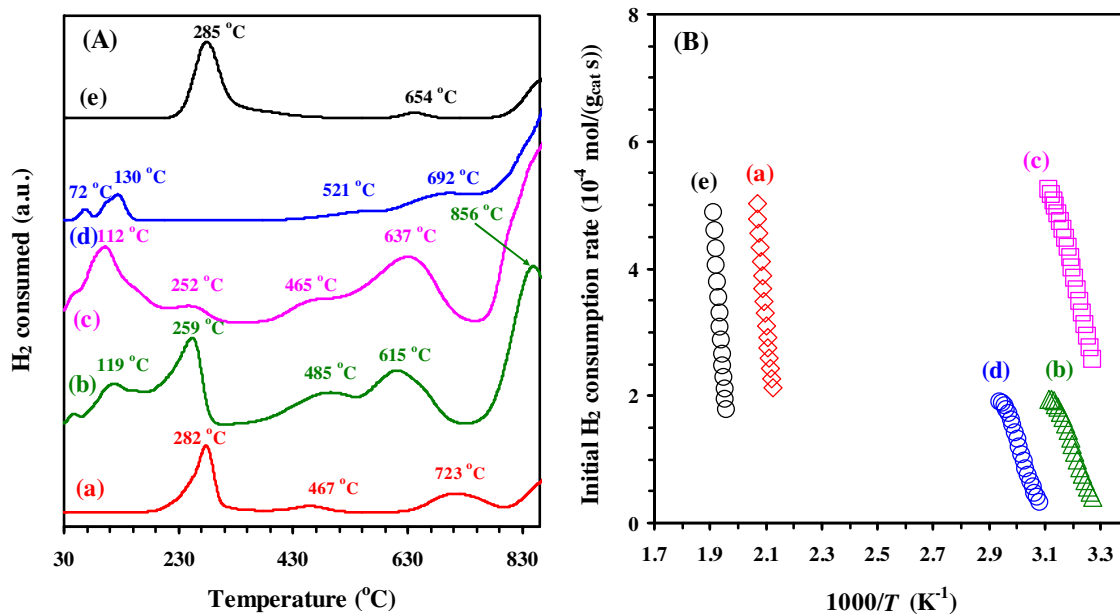


Fig. 7. (A) H₂-TPR profiles and (B) initial H₂ consumption rate as a function of inverse temperature of (a) 3DOM CoCr₂O₄, (b) 0.98AuPd_{1.93}/3DOM CoCr₂O₄, (c) 1.93AuPd_{1.95}/3DOM CoCr₂O₄, (d) 1.98AuPd_{1.96}/Bulk CoCr₂O₄, and (e) Bulk CoCr₂O₄.

Table 3

Catalytic activities, TOF values, and specific reaction rates of the samples at SV = 20,000 mL/(g h).

| Sample | Methane combustion activity | | | Methane combustion at 320 °C | | |
|---|-----------------------------|-----------------------|-----------------------|--|---|---|
| | T _{10%} (°C) | T _{50%} (°C) | T _{90%} (°C) | TOF _{Noblemetal} ($\times 10^{-3}$ s ⁻¹) | TOF _{CoCr2O4} ($\times 10^{-3}$ s ⁻¹) | Specific reaction rate ($\mu\text{mol}/(\text{g}_{\text{cat}} \text{s})$) |
| 3DOM CoCr ₂ O ₄ | 320 | 370 | 440 | – | 0.168 | 0.744 |
| 0.98AuPd _{1.93} /3DOM CoCr ₂ O ₄ | 310 | 362 | 410 | 13.0 | 0.213 | 0.931 |
| 1.93AuPd _{1.95} /3DOM CoCr ₂ O ₄ | 305 | 353 | 394 | 8.23 | 0.271 | 1.15 |
| 1.98AuPd _{1.96} /Bulk CoCr ₂ O ₄ | 325 | 385 | 467 | 3.75 | 0.123 | 0.541 |
| Bulk CoCr ₂ O ₄ | 335 | 400 | 490 | – | 0.0936 | 0.413 |

compare the activities of all of the samples, we use the reaction temperatures (T_{10%}, T_{50%}, and T_{90%}) at methane conversion = 10, 50, and 90%, respectively, as summarized in Table 3. Among these samples, the 1.93AuPd_{1.95}/3DOM CoCr₂O₄ sample performed the best: T_{10%} = 305 °C, T_{50%} = 353 °C, and T_{90%} = 394 °C at SV = 20,000 mL/(g h). Obviously, the T_{90%} over 1.93AuPd_{1.95}/3DOM CoCr₂O₄ was lower

by 16, 46, 73, and 96 °C than those over 0.98AuPd_{1.93}/3DOM CoCr₂O₄, 3DOM CoCr₂O₄, 1.98AuPd_{1.96}/Bulk CoCr₂O₄, and Bulk CoCr₂O₄, respectively. Compared to 0.98AuPd_{1.93}/3DOM CoCr₂O₄ or 1.98AuPd_{1.96}/Bulk CoCr₂O₄, 1.93AuPd_{1.95}/3DOM CoCr₂O₄ possessed higher surface O_{ads}/O_{latt}, Au^{δ+}/Au⁰, and Pd²⁺/Pd⁰ molar ratios (Table 2). It is well known that a larger amount of surface

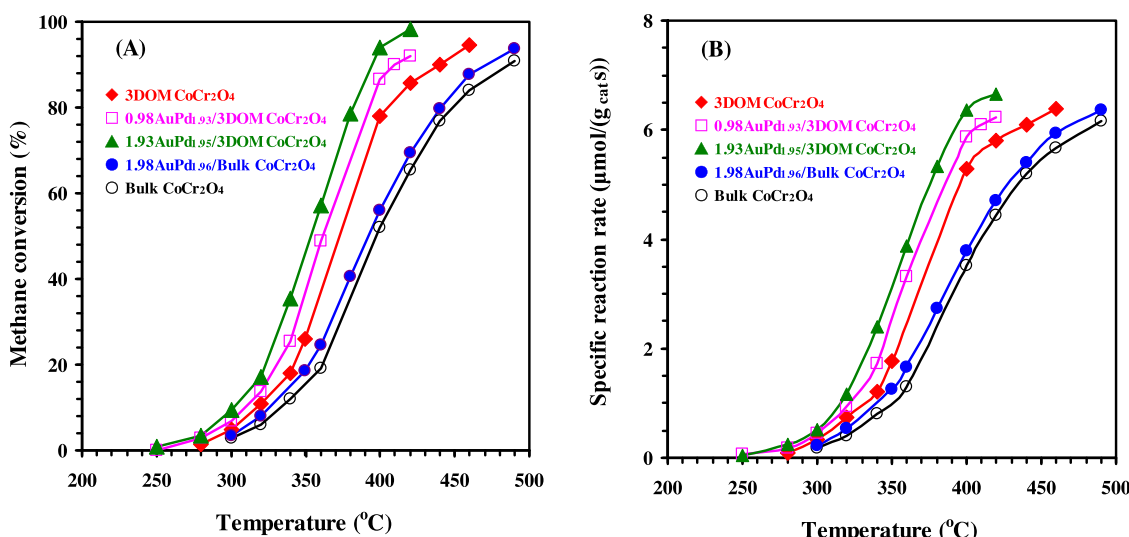


Fig. 8. (A) Methane conversion and (B) specific reaction rate as a function of reaction temperature over the as-prepared samples at SV = 20,000 mL/(g h).

adsorbed oxygen species benefits the adsorption and activation of reactants [29], and higher surface $\text{Au}^{\delta+}/\text{Au}^0$ and $\text{Pd}^{2+}/\text{Pd}^0$ molar ratios could improve the low-temperature reducibility (Fig. 7). Therefore, we believe that the better catalytic performance of 1.93AuPd_{1.95}/3DOM CoCr₂O₄ might be associated with its surface element compositions and low-temperature reducibility.

As we know, there are several kinds of active sites (e.g., noble metal, transition-metal mixed oxide, and interface between noble metal NPs and transition-metal mixed oxide) in the reducible mixed metal oxide-supported noble metal catalysts. Thus, it is hard to calculate the turnover frequencies (TOFs). The TOF_M ($\text{TOF}_M = zC_0/n_M$, where z is the conversion at a certain temperature, C_0 (mol/s) is the initial methane concentration per second, and n_M (mol) is the molar amount of metal or mixed oxide ($M=\text{Au-Pd}$ or CoCr_2O_4) and specific reaction rates normalized per gram of catalyst or noble metals at a typical temperature (e.g., 320 °C) were calculated according to the activity data and amounts of Au-Pd and CoCr₂O₄ in the samples, as summarized in Table 3. It is seen that the highest $\text{TOF}_{\text{Noble metal}}$ ($13.0 \times 10^{-3} \text{ s}^{-1}$) was achieved over the 0.98AuPd_{1.93}/3DOM CoCr₂O₄ sample (possible due to the lower loading of noble metals), whereas the highest $\text{TOF}_{\text{CoCr}_2\text{O}_4}$ ($0.271 \times 10^{-3} \text{ s}^{-1}$) was obtained over the 1.93AuPd_{1.95}/3DOM CoCr₂O₄ sample. According to the XPS and H₂-TPR results (Figs. 6 and 7 and Table 2), we deduce that there was a synergistic effect between Au-Pd NPs and 3DOM CoCr₂O₄. As shown in Table 3, the TOFs normalized by the amount of noble metal were larger than the TOFs normalized by the amount of CoCr₂O₄, indicating that noble metal NPs were more active than CoCr₂O₄. On the other hand, the TOFs normalized by the amount of noble metal were quite different for the Au-Pd supported catalysts, suggesting that CH₄ oxidation might not occur predominantly on the noble metal sites. Hence, we believe that the synergistic effect between Au-Pd NPs and 3DOM CoCr₂O₄ played an important role in the oxidation of CH₄. Fig. 8B shows the specific reaction rates normalized per gram of catalyst. The changing trends in methane reaction rate versus temperature were similar to those in methane conversion versus temperature, and the 1.93AuPd_{1.95}/3DOM CoCr₂O₄ sample exhibited the highest specific reaction rate ($1.15 \mu\text{mol}/(\text{g}_{\text{cat}} \text{s})$) at 320 °C, although the highest specific reaction rate ($95.0 \mu\text{mol}/(\text{g}_{\text{Nobl metal}} \text{s})$) at 320 °C was achieved over the 0.98AuPd_{1.93}/3DOM CoCr₂O₄ sample.

In order to examine the catalytic stability, we carried out the 40-h on-stream methane oxidation over the best-performing 1.93AuPd_{1.95}/3DOM CoCr₂O₄ sample at 394 °C and $\text{SV}=20,000 \text{ mL}/(\text{g h})$, and the result is shown in Fig. 9. No significant loss in catalytic activity was observed. In other words, the 1.93AuPd_{1.95}/3DOM CoCr₂O₄ sample was catalytically durable under the adopted conditions.

In the past years, methane combustion over various supported noble metal catalysts has been reported. It is worth pointing out that $x\text{AuPd}/3\text{DOM CoCr}_2\text{O}_4$ were superior in catalytic methane combustion to 1 wt% Pd/ZrO₂ [39], 4.5 wt% Ru/ZnAl₂O₄ [40], 3 wt% Ce30Cr-500/Al₂O₃ [41], Pd-PdO_x-Pt/Al₂O₃ [42], and La_{0.6}Sr_{0.4}MnO₃ [43].

3.5. Effects of SV, water vapor, and sulfur dioxide

The effect of SV on methane combustion over the 1.93AuPd_{1.95}/3DOM CoCr₂O₄ sample is shown in Fig. 10. It is observed that methane conversion decreased with the rise in SV, a result due to the shortening of contact time.

On-stream methane combustion over the 1.93AuPd_{1.95}/3DOM CoCr₂O₄ sample in the presence and absence of 5.0 vol% water vapor at 378 °C and $\text{SV}=20,000 \text{ mL}/(\text{g h})$ was conducted to examine the effect of moisture on catalytic activity, and the result is shown in Fig. 11. It is found that when 5.0 vol% water vapor was

introduced to the feedstock, methane conversion decreased from ca. 76–69%; when water vapor was cut off, methane conversion restored to the original value. The deactivation of this sample in the presence of water vapor might be due to the competitive adsorption of water and methane molecules on the surface of the sample. Therefore, introduction of moisture exerted a negative effect on methane combustion, and the deactivation due to water vapor addition was reversible. Similar phenomena have been reported by other researchers [4,19–21].

Fig. 12 shows the effect of SO₂ on methane combustion over 1.93AuPd_{1.95}/3DOM CoCr₂O₄ at 394 °C and $\text{SV}=20,000 \text{ mL}/(\text{g h})$ in the presence of 100 ppm SO₂. It can be seen from Fig. 12, that methane conversion slowly decreased from 90 to 80% after 20 h of on-stream reaction. After the used sample was activated in O₂ at 500 °C for 1 h, methane conversion slightly increased to ca. 85%. This result demonstrates that deactivation of the 1.93AuPd_{1.95}/3DOM CoCr₂O₄ sample induced by SO₂ addition was irreversible. Wu et al. [20] reported that the SO₂ introduced to the supported pal-

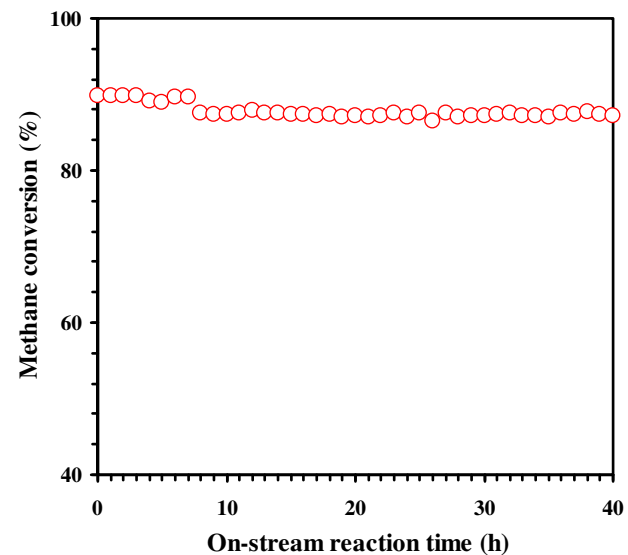


Fig. 9. Methane conversion as a function of on-stream reaction time over the 1.93AuPd_{1.95}/3DOM CoCr₂O₄ sample at 394 °C and $\text{SV}=20,000 \text{ mL}/(\text{g h})$.

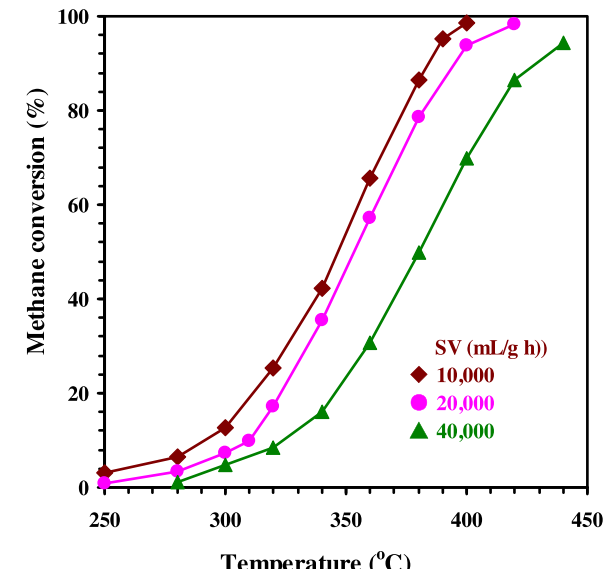


Fig. 10. Effect of SV on methane combustion over the 1.93AuPd_{1.95}/3DOM CoCr₂O₄ sample.

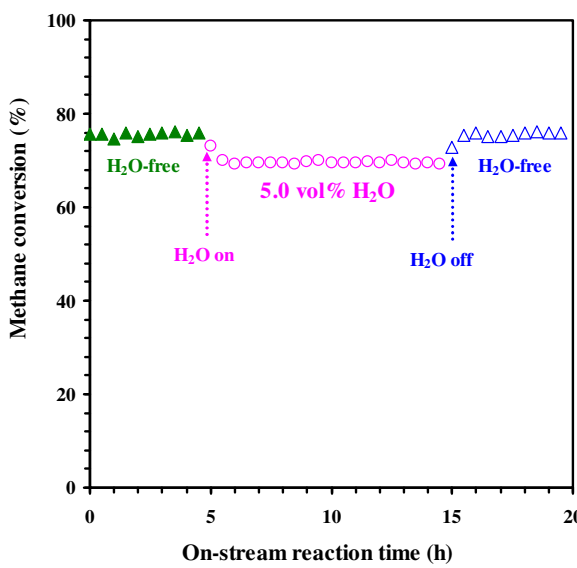


Fig. 11. Effect of water vapor on methane conversion over the 1.93AuPd_{1.95}/3DOM CoCr₂O₄ sample at 378 °C and SV = 20,000 mL/(g h).

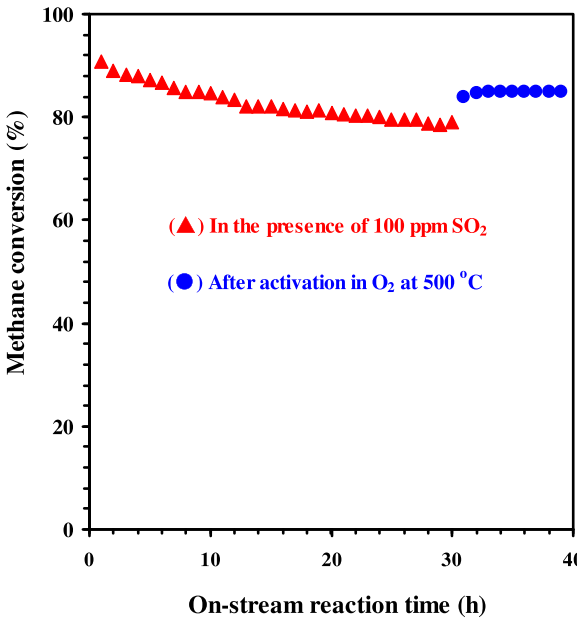


Fig. 12. Effect of SO₂ on methane conversion over the 1.93AuPd_{1.95}/3DOM CoCr₂O₄ sample at 394 °C and SV = 20,000 mL/(g h).

ladium catalyst could lead to formation of the SO₃²⁻ or SO₄²⁻ species: SO₂ + PdO → PdSO₃ or PdSO₄ [44]. The slight rise (ca. 5%) in methane conversion over the activated sample might be due to decomposition of the generated unstable sulfite PdSO₃ species: PdSO₃ + O₂ → PdO + SO₂.

4. Conclusions

The 3DOM CoCr₂O₄ and xAuPd_y/3DOM CoCr₂O₄ samples with a surface area of 33–36 m²/g could be prepared using the PMMA-templating and PVA-protected reduction methods, respectively. The 3DOM CoCr₂O₄ in the samples was cubic in crystal structure and possessed a high-quality 3DOM architecture. The Au–Pd alloy NPs with an average particle size of 3.3 nm were uniformly dispersed on the surface of the samples. Among all of the samples, the 1.93AuPd_{1.95}/3DOM CoCr₂O₄ sample exhibited the best

low-temperature reducibility and the highest adsorbed oxygen species concentration, rendering it to show the best catalytic performance ($T_{50\%} = 353$ °C and $T_{90\%} = 394$ °C) for methane combustion at SV = 20,000 mL/(g h). The addition of moisture and sulfur dioxide to the reaction system gave rise to deactivation of the 1.93AuPd_{1.95}/3DOM CoCr₂O₄ sample, the deactivation induced by water vapor addition was reversible but SO₂ introduction caused irreversible deactivation. It is concluded that the excellent catalytic performance of 1.93AuPd_{1.95}/3DOM CoCr₂O₄ was associated with its high surface area and O_{ads} concentration, good low-temperature reducibility, and strong interaction between Au–Pd alloy NPs and 3DOM CoCr₂O₄.

Acknowledgments

This work was supported by the NSF of China (21377008 and 21477005), National High Technology Research and Development Program of China (2015AA034603), Beijing Nova Program (Z141109001814106), NSF of Beijing Municipal Commission of Education (KM201410005008), Foundation on the Creative Research Team Construction Promotion Project of Beijing Municipal Institutions, and Scientific Research Base Construction–Science and Technology Creation Platform National Materials Research Base Construction.

References

- [1] P. Gelin, M. Primet, *Appl. Catal. B* 39 (2002) 1–37.
- [2] L.H. Hu, Q. Peng, Y.D. Li, *ChemCatChem* 3 (2011) 868–874.
- [3] J. Xu, L.K. Ouyang, W. Mao, X.J. Yang, X.C. Xu, J.J. Su, T.Z. Zhuang, H. Li, Y.F. Han, *ACS Catal.* 2 (2012) 261–269.
- [4] W. Tan, J.G. Deng, S.H. Xie, H.G. Yang, Y. Jiang, G.S. Guo, H.X. Dai, *Nanoscale* 7 (2015) 8510–8523.
- [5] D. Nepak, S. Darbha, *Catal. Commun.* 58 (2015) 149–153.
- [6] M.S. Chen, D. Kumar, C.W. Yi, D.W. Goodman, *Science* 310 (2005) 291–293.
- [7] D.I. Enache, J.K. Edwards, P. Landon, B. Solsona-Espriu, A.F. Carley, A.A. Herzing, M. Watanabe, C.J. Kiely, D.W. Knight, G.J. Hutchings, *Science* 311 (2006) 362–365.
- [8] G. Ercolino, G. Grzybek, P. Stelmachowski, S. Specchia, A. Kotarba, V. Specchia, *Catal. Today* 257 (2015) 66–71.
- [9] M.M. Fiuk, A. Adamski, *Catal. Today* 257 (2015) 131–135.
- [10] A. Setiawan, E.M. Kennedy, B.Z. Dlugogorski, A.A. Adesina, M. Stockenhuber, *Catal. Today* 258 (2015) 276–283.
- [11] Y. Wang, A.P. Jia, M.F. Luo, J.Q. Lu, *Appl. Catal. B* 165 (2015) 477–486.
- [12] J. Słoczyński, J. Janas, T. Machej, J. Rynkowski, J. Stoch, *Appl. Catal. B* 24 (2000) 45–60.
- [13] J.N. Hu, W.Y. Zhao, R.S. Hu, G.Y. Chang, C. Li, L.J. Wang, *Mater. Res. Bull.* 57 (2014) 268–273.
- [14] J.H. Chen, X.Y. Zhang, H. Arandiyan, Y. Peng, H.Z. Chang, J.H. Li, *Catal. Today* 201 (2013) 12–18.
- [15] J.H. Chen, W.B. Shi, X.Y. Zhang, H. Arandiyan, D.F. Li, J.H. Li, *Environ. Sci. Technol.* 45 (2011) 8491–8497.
- [16] X.D. Meng, R. Al-Salman, J.P. Zhao, N. Borissenko, Y. Li, F. Endres, *Angew. Chem. Int. Ed.* 48 (2009) 2703–2707.
- [17] Z.Q. Tong, J. Hao, K. Zhang, J.P. Zhao, B.L. Su, Y. Li, *J. Mater. Chem. C* 2 (2014) 3651–3658.
- [18] S.H. Xie, J.G. Deng, Y.X. Liu, Z.H. Zhang, H.G. Yang, Y. Jiang, H. Arandiyan, H.X. Dai, C.T. Au, *Appl. Catal. A* 507 (2015) 82–90.
- [19] S.H. Xie, J.G. Deng, S.M. Zang, H.G. Yang, G.S. Guo, H. Arandiyan, H.X. Dai, *J. Catal.* 322 (2015) 38–48.
- [20] Z.X. Wu, J.G. Deng, Y.X. Liu, S.H. Xie, Y. Jiang, X.T. Zhao, J. Yang, H. Arandiyan, G.S. Guo, H.X. Dai, *J. Catal.* 332 (2015) 13–24.
- [21] S.H. Xie, J.G. Deng, Y.X. Liu, Z.H. Zhang, H.G. Yang, Y. Jiang, H. Arandiyan, H.X. Dai, C.T. Au, *Appl. Catal. A* 507 (2015) 82–90.
- [22] X.W. Li, H.X. Dai, J.G. Deng, Y.X. Liu, S.H. Xie, Z.X. Zhao, Y. Wang, G.S. Guo, H. Arandiyan, *Chem. Eng. J.* 228 (2013) 965–975.
- [23] L.F. Liotta, C. Di Carlo, G. Pantaleo, A.M. Venezia, G. Deganello, *Appl. Catal. B* 66 (2006) 217–227.
- [24] Y.J. Feng, L. Li, S.F. Niu, Y. Qu, Q. Zhang, Y.S. Li, W.R. Zhao, H. Li, J.L. Shi, *Appl. Catal. B* 111–112 (2012) 461–466.
- [25] Y.X. Lin, W.P. Cai, X.Y. Tian, X.L. Liu, G.Z. Wang, C.H. Liang, *J. Mater. Chem.* 21 (2011) 991–997.
- [26] X.W. Xie, Y. Li, Z.Q. Liu, M. Haruta, W.J. Shen, *Nature* 458 (2009) 746–749.
- [27] D.C. Kim, S.K. Ihm, *Environ. Sci. Technol.* 35 (2001) 222–226.
- [28] J. Słoczyński, J. Janas, T. Machej, J. Rynkowski, J. Stoch, *Appl. Catal. B* 24 (2000) 45–60.

- [29] S. Rousseau, S. Lordinat, P. Delichere, A. Boreave, J.P. Deloume, P. Vernoux, *Appl. Catal. B* 88 (2009) 438–447.
- [30] S. Ponce, M.A. Peña, J.L.G. Fierro, *Appl. Catal. B* 24 (2000) 193–205.
- [31] Y.C. Wei, J. Liu, Z. Zhao, Y.S. Chen, C.M. Xu, A.J. Duan, G.Y. Jiang, H. He, *Angew. Chem. Int. Ed.* 50 (2011) 2326–2329.
- [32] Y.X. Liu, H.X. Dai, J.G. Deng, L. Zhang, B.Z. Gao, Y. Wang, X.W. Li, S.H. Xie, G.S. Guo, *Appl. Catal. B* 140–141 (2013) 317–326.
- [33] S.Y. Huang, C.B. Zhang, H. He, *J. Environ. Sci.* 25 (2013) 1206–1212.
- [34] Y.X. Liu, H.X. Dai, J.G. Deng, X.W. Li, Y. Wang, H. Arandian, S.H. Xie, H.G. Yang, G.S. Guo, *J. Catal.* 305 (2013) 146–153.
- [35] P. Bracconi, L.C. Dufour, *J. Phys. Chem.* 79 (1975) 2400–2405.
- [36] D.C. Kim, S.K. Ihm, *Environ. Sci. Technol.* 35 (2001) 222–226.
- [37] B. Grzybowska, J. Słoczyński, R. Grabowski, K. Wcislo, A. Kozłowska, J. Stoch, J. Zieliński, *J. Catal.* 178 (1998) 687–700.
- [38] K.D. Chen, S.B. Xie, A.T. Bell, E. Iglesia, *J. Catal.* 198 (2001) 232–242.
- [39] S.W. Yang, A. Maroto-Valiente, M. Benito-Gonzalez, I. Rodriguez-Ramos, A. Guerrero-Ruiz, *Appl. Catal. B* 28 (2000) 223–233.
- [40] J. Okal, M. Zawadzki, K. Baranowska, *Appl. Catal. A* 471 (2014) 98–105.
- [41] X.Z. Yuan, S.Y. Chen, H. Chen, Y.C. Zhang, *Catal. Commun.* 35 (2013) 36–39.
- [42] N.M. Kinnunen, J.T. Hirvi, M. Suvanto, T.A. Pakkanen, *J. Mol. Catal. A* 356 (2012) 20–28.
- [43] H. Arandian, H.X. Dai, J.G. Deng, Y.X. Liu, B.Y. Bai, Y. Wang, X.W. Li, S.H. Xie, J.H. Li, *J. Catal.* 307 (2013) 327–339.
- [44] D.L. Mowery, R.L. McCormick, *Appl. Catal. B* 34 (2001) 287–297.